Journal of Molecular Structure 1229 (2021) 129844

Contents lists available at ScienceDirect

Journal of Molecular Structure

journal homepage: www.elsevier.com/locate/molstr

Experimental and theoretical study on spectral features, reactivity, solvation, topoisomerase I inhibition and *in vitro* cytotoxicity in human HepG2 cells of guadiscine and guadiscidine aporphine alkaloids

Renyer A. Costa[a,*], Gabriel de A. Barros[b], Jonathas N. da Silva[c], Kelson M. Oliveira[a], Daniel P. Bezerra[d], Milena B.P. Soares[d], Emmanoel V. Costa[a,*]

[a] Department of Chemistry, Federal University of Amazonas (DQ-UFAM), 69080-900 Manaus, AM, Brazil
[b] Chemistry institute, University of Campinas, 13083-861 Campinas-SP, Brazil
[c] Faculty of Sciences and Letters - Araraquara Campus, São Paulo State University (UNESP), São Paulo, SP 1400901, Brazil
[d] Gonçalo Moniz Institute, Oswaldo Cruz Fundation (IGM/FIOCRUZ-BA), Salvador, Bahia, Brazil

ARTICLE INFO

Article history:
Received 29 October 2020
Revised 15 December 2020
Accepted 22 December 2020
Available online 29 December 2020

Keywords:
DFT
7,7-dimethylaporphine alkaloids
Docking
Molecular dynamics
Cytotoxicity
HepG2

ABSTRACT

In this study, guadiscine (G1) and guadiscidine (G2), 7,7-dimethylaporphine alkaloids from *Guatteria friesiana*, have they geometric paramaters, vibrational behavior and quantum chemical properties (HOMO-LUMO, MEP, ALIE and Fukui indices) analyzed through a theoretical view, by density functional theory (DFT), using the Becker's three-parameter hybrid exchange functional combined with the Lee–Yang–Parr correlation functional (B3LYP) and 6–311G(2d,p) and 6–311G++(2df,3p) basis sets. The obtained geometry data were compared with x-ray data for (−)-*N*-acetyl-anonaine, showing close values. Vibrational analysis, together with potential energy distribution (PED) calculations, revealed several characteristic vibrations that characterize the 7,7 dimethylaporphine skeleton, besides enabling the observation of intermolecular H-bonds through dimers formation. Molecular dynamic simulations were carried out, allowing to evaluate the solvation free energies of G1 and G2 in water, methanol and ethanol, as well as H-bonds formation between G1 and G2 and the tested solvents. The antineoplastic potential of the title molecules was evaluated via molecular docking calculations with topoisomerase I complexed with DNA. Guadiscine and guadiscidine showed, respectively, binding free energies of -8.0 and -8.5 kcal/mol, while topotecan, a DNA topoisomerase I inhibitor, showed a binding free energy value of -12 kcal/mol, indicating that the studied molecules are good topoisomerase I inhibitors. *In vitro* cytotoxicity assay with HepG2 cell line were performed, revealing significant antitumor potential for G2.

1. Introduction

Aporphinoid alkaloids are a group of plant secondary metabolites that present many biological activities such as trypanocidal [1], antiinflamatory [2], antifungal [3], antioxidant [4], cytotoxic [5,6] and antibactericidal [7]. A main source of such metabolites is the *Annonaceae* family, in which the *Guatteria* genus is the largest one, with more than 300 species in neotropical distribution and highest diversity on Amazonian region [8]. In this context, guadiscine (G1) and guadiscidine (G2) (Fig. 1), 6,6a-dehydro-7,7-dimethylaporphine alkaloids [9], attract attention to be chemotaxonomic markers of *Guatteria* genus plants [10], in which G1 exhibit certain antimicrobial [11,12] and cytotoxic activities [10]. With regard to G2, its biological properties are unknown so far, and, for both structures, their structural, vibrational and quantum chemical properties had not yet been fully investigated.

In this work, these two alkaloids, G1 and G2, previously isolated from *Guatteria friesiana* [9], were evaluated through a theoretical view (geometry optimization, HOMO-LUMO, vibrational behavior, UV-vis, Fukui functions, MEP and ALIE calculations) via density functional theory (DFT) using 6–311G(2d, p) and 6–311G++(2df, 3p) basis sets, where the obtained data were compared to the experimental ones, providing a more complete description of the properties of these structures. In view of the evaluation of the solvation energies and the interactions between the alkaloids atoms and solvent atoms, molecular dynamic simulations were carried out. Furthermore, guided by cytotoxic properties presented by the position 7-substituted aporphine alkaloids [13-17], molecular docking calculations were performed in front of topoisomerase I enzyme to evaluate their inhibition capacity. *In vitro* cytotoxicity as-

* Corresponding authors.
E-mail address: renyer.costa@gmail.com (R.A. Costa).

https://doi.org/10.1016/j.molstruc.2020.129844
0022-2860/

say with HepG2 cell line for G2 is also reported and compared to G1. To the best of our knowledge, no theoretical molecular modeling study that discusses the geometry, HOMO-LUMO energies, MEP and ALIE surfaces, interaction with different solvents (by radial distribution function analysis), solvation free energies and docking analysis with topoisomerase I has been presented yet.

2. Methodology

2.1. Experimental details

Pure samples of G1 and G2 alkaloids were provided by the Research group on chemical studies of biomolecules (acronym in Portuguese GEQBiom) of Federal University of Amazonas. The isolation methods and structural elucidation by NMR spectroscopy were described in previous work [9]. However, as a proof, the NMR data of the studied molecules are found in the supplementary material (Fig S1–18). The FT-IR spectra of guadiscine (G1) and guadiscidine (G2) crystals were recorded on a Shimadzu IR Prestige-21 spectrometer, and UV−Vis spectra were measured on an Agilent HP 8453 spectrophotometer, with G1 and G2 crystals solubilized in methanol.

2.2. Computational methods

2.2.1. DFT calculations

The theoretical calculations were performed using the Gaussian 09 Program (Revision E.01) [18] via DFT approach using 6–311G(2d, p) and 6–311G++(2df,3p) basis sets and the B3LYP hybrid functional (for geometry optimization, HOMO-LUMO energies, Fukui indices and IR spectra). Molecular electrostatic potential (MEP) and average local ionization energy (ALIE) surfaces were generated using the Multiwfn program [19]. The theoretical IR spectra were obtained from the DFT intensities in combination with the calculated vibrational wavenumbers, which were scaled by 0.96 (for frequencies higher than 1800 cm $^{-1}$) and 0.98 (for frequencies up to 1800 cm^{-1}). No imaginary frequencies or negative eigenvalues were registered. The potential energy distribution (PED) was calculated with the help of VEDA4 software package [20]. The UV spectra were calculated using the B3LYP functional with 6–311G++(2df,3p) basis set in methanol via PCM/TD-DFT approach.

2.2.2. Molecular docking calculations

Molecular docking calculations were performed with the help of AutoDock Vina software [21]. DNA topoisomerase I complex with topotecan was achieved from Protein Data Bank (PDB) website with PDB ID 1K4T [22]. The calculation protocol consisted in removing water molecules and co-crystallized ligand (topotecan), Gasteiger charges were added, and a gridbox was centralized at the active site, with dimensions based on previous works [23,24]. The docking protocol was validated removing the co-crystallized topotecan and then docking at the same site with the proposed gridbox. The superimposition of the structures showed RMSD of 0.80 for the topoisomerase I inhibitor. RMSD values up to 2 Å are considered reliable for a docking protocol.

2.2.3. Molecular dynamic simulations

For molecular dynamic (MD) calculations, all molecules were set up using the official CHARMM General Force Field (CGenFF) server [25], and the TIP3 model was used for water. CHARMM36 force field [26], with the help of GROMACS package version 2019 [27], was used in the simulations. Particle Mesh Ewald (PME) [28] was used to calculate the long-range ionic interactions. The covalent bonds in which hydrogen atoms are present were constrained by LINCS (Linear Constraint Solver) [29]. For each system, a 50,000-step minimization was used followed by 125 ps equilibration runs with 1 fs step size. The final step was the production of NTP (constant pressure/temperature) simulation at 300 K using 2 fs time steps for 12 ns. The reference pressure (1 bar) was controlled using the Berendsen method [29] with a coupling every 2 ps. Temperature was controlled using the modified Berendsen thermostat [30] with coupling every 0.1 ps. The MD simulations consisted in putting one molecule in three different boxes containing approximately 1250 water molecules, 1000 methanol molecules and 900 ethanol molecules. For both molecules, the grid box dimensions used were 35, 112 and 120 nm^3 for water, methanol and ethanol respectively.

2.3. In vitro *cytotoxicity assay*

Human hepatocellular carcinoma (HepG2) cell line was obtained from the American Type Culture Collection (ATCC, Manassas, VA, USA). Mycoplasma Stain Kit (Sigma-Aldrich) was used to test HepG2 cells for mycoplasma reassuring lack of contamination. Cell viability was measured by alamar blue assay and performed as previously reported [31]. Doxorrubicin was used as positive control. The half-maximum inhibitory concentration (IC_{50}) and their respective 95% confidence intervals were calculated by non-linear regression using the GraphPad Prism (Intuitive Software for Science; San Diego, CA, USA).

3. Results

3.1. Geometry optimization

The theoretical geometry optimization results of the studied molecules G1 and G2 (Fig. 1) calculated at DFT B3LYP/6–311*G*++(2df,3p) level of theory were compared with X-ray data of (−)-*N*-acetyl-anonaine presented in literature [32] (see Table 1). Both molecules showed C1 symmetry with the most stable conformations showing electronic energy values of −1054.26079 and −1014.94959 a.u. respectively. The RMSD (Root Mean Square Deviation) between the experimental reference data and the theoretical ones are 0.0150 and 0.0148 Å, for G1 and G2 respectively, in respect to the interatomic distances, and 3.2612° and 3.2645°, respectively, for the bond angles.

Geometry parameters of both structures indicates uniformity on Rings A and D bond lengths, showing values around ~1.38 Å, except for the bonds C3a-C3b (1.39 Å for both structures) and C3b-C1a (1.42 Å for both structures). Rings B (2,3 dihydropyridine) and C show non-uniformity in their geometry, fact that is justified by different values for all bond lengths, being noteworthy N6-C6 (1.27 Å), C4-C5 (1.52 Å), C3a-C4 (1.51 Å), C1a-C11a (1.47 Å) and C7-C7a (1.53 Å). Concerning to the bond angles, in both structures, rings A and D showed uniformity, revealing values around ~122°, except for the bond angles 116.6° (C2-C3-C3a), 114.7° (C3b-C1a-C1), 119.3° (C11a-C7a-C8 for G1), 118.9° (C11a-C7a-C8 for G2) and 118.5° (C11-C11a-C7a). Concerning to rings B and C, for both structures, distortions in all angles were observed, such as 117.1° (C3b-C3a-C4), 109.5° (C3a-C4-C5), 123.4° (N6-C6a-C3b), 119.8° (C3b-C1a-

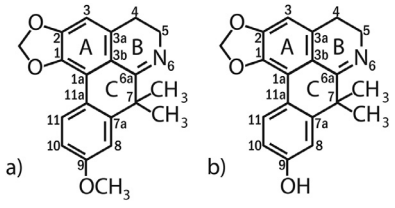

Fig. 1. Structures of (a) G1 and (b) G2.

Table 1
Bonds lengths (Å) and angles calculated for guadiscine and guadiscidine at DFT B3LYP/6–311G++(2df,3p) level of theory.

Parameter Bond lengths (Å)	Guadiscine	Guadiscidine	Experimental [32]	Parameter Bond angles (°)	Guadiscine	Guadiscidine	Experimental [32]
C1-C2	1.387	1.387	1.394	C1a-C1-C2	122.52	122.52	122.8
C2-C3	1.375	1.375	1.360	C1-C2-C3	122.84	122.83	122.0
C3-C3a	1.397	1.397	1.410	C2-C3-C3a	116.59	116.61	177.4
C3a-C3b	1.399	1.399	1.398	C3-C3a-C3b	120.77	120.77	120.3
C3b-C1a	1.420	1.420	1.428	C3a-C3b-C1a	122.56	122.53	122.0
C1-C1a	1.387	1.387	1.372	C3b-C1a-C1	114.67	114.70	115.2
C3a-C4	1.506	1.506	1.514	C3b-C3a-C4	117.09	117.09	119.5
C4-C5	1.525	1.525	1.505	C3a-C4-C5	109.47	109.47	110.0
C5-N6	1.460	1.461	–	C4-C5-N6	112.74	112.72	109.5
N6-C6a	1.276	1.275	–	C5-N6-C6a	117.55	117.53	116.0
C3b-C6a	1.478	1.475	1.506	N6-C6a-C3b	123.44	123.46	112.2
C6a-C7	1.530	1.531	1.525	C6a-C3b-C3a	117.92	117.89	122.8
C7-C7a	1.533	1.532	1.502	C3b-C1a-C11a	119.81	119.81	120.2
C7a-C11a	1.407	1.410	1.405	C1a-C3b-C6a	119.52	119.57	115.2
C1a-C11a	1.470	1.470	1.485	C3b-C6a-C7	116.91	116.91	110.3
C7a-C8	1.396	1.392	1.398	C6a-C7-C7a	110.18	110.09	109.6
C8-C9	1.392	1.391	1.376	C7-C7a-C11a	120.61	120.69	120.0
C9-C10	1.394	1.388	1.380	C7a-C11a-C1a	119.86	119.70	118.4
C10-C11	1.379	1.383	1.380	C11a-C7a-C8	119.29	118.91	118.8
C11-C11a	1.405	1.403	1.400	C7a-C8-C9	121.26	121.50	121.6
C9-O	1.361	1.365	–	C8-C9-C10	119.57	119.92	120.0
RMSD	0.0150	0.0148		C9-C10-C11	119.54	119.10	119.7
				C10-C11-C11a	121.82	121.97	120.8
				C11-C11a-C7a	118.51	118.61	119.1
				RMSD	3.2612	3.2645	

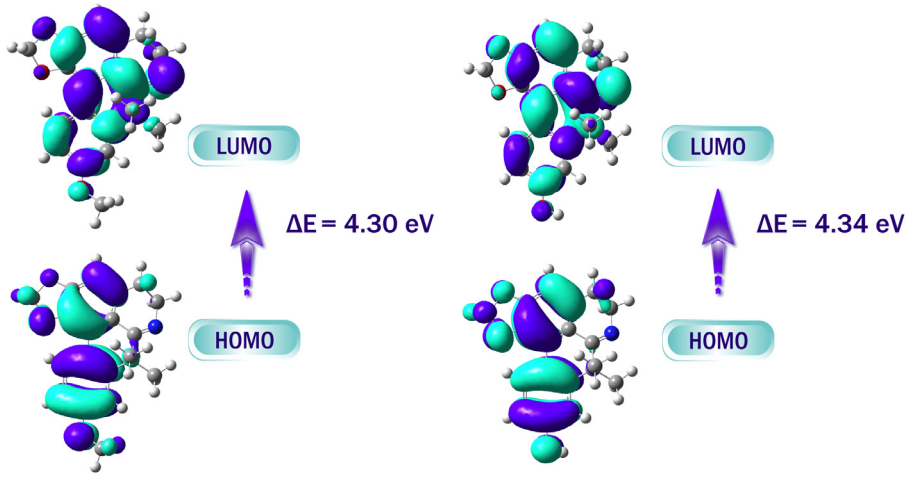

Fig. 2. Frontier molecular orbitals of G1 (left) and G2 (right) using DFT approach.

C11a), 110.2° (C6a-C7-C7a) and 120.6° (C7-C7a-C11a). Rings B and C present conformations that resembles half-chair conformation due to the unsaturations, which can be verified by the dihedral angles values −52.611° (C3a-C4-C5-N6) and 40.106° (C3b-C6a-C7-C7a) for G1 and −52.65° (C3a-C4-C5-N6) and 40.20° (C3b-C6a-C7-C7a) for G2.

3.2. Frontier orbitals analysis

The highest occupied molecular orbitals (HOMO) and the lowest-lying unoccupied molecular orbitals (LUMO), also called frontier molecular orbitals (FMOs), act as an essential part in quantum chemistry calculations. These orbitals are an indispensable tool for the description of chemical behavior, such as charge transfer, reaction pathways and molecular electronics [33-35]. The calculated molecular orbitals (MOs) for G1 and G2 as well as the HOMO/LUMO energy gaps are shown in Fig. 2.

According to Janak theorem and Perdew et al. demonstration for a Z-electron system, $\varepsilon i = -$ IP ($Z - 1 < N < Z$) and $\varepsilon i = -$ EA ($Z < N < Z + 1$), where εi is the corresponding KS orbital energy, I is the ionization potential of the molecule, being $I = -E_{HOMO}$, and A is the electron affinity, being $A = -E_{LUMO,}$ it's possible to calculate the very useful global reactivity parameters, hardness (η), chemical potential (μ), electronegativity (χ) and electrophilicity index (ω), which, based on Koopmans theorem for closed-shell molecules in Hartree-Fock approach, are given as [36,37]:

$$-\mu = \chi = -\left(\frac{\partial E}{\partial N}\right)_V = \frac{-(I+A)}{2}$$

$$\eta = \frac{1}{2}\left(\frac{\partial \mu}{\partial N}\right)_V = \frac{1}{2}\left(\frac{\partial^2 E}{\partial N^2}\right) = \frac{(I-A)}{2}$$

$$\omega = \left(\frac{\mu^2}{2\eta}\right)$$

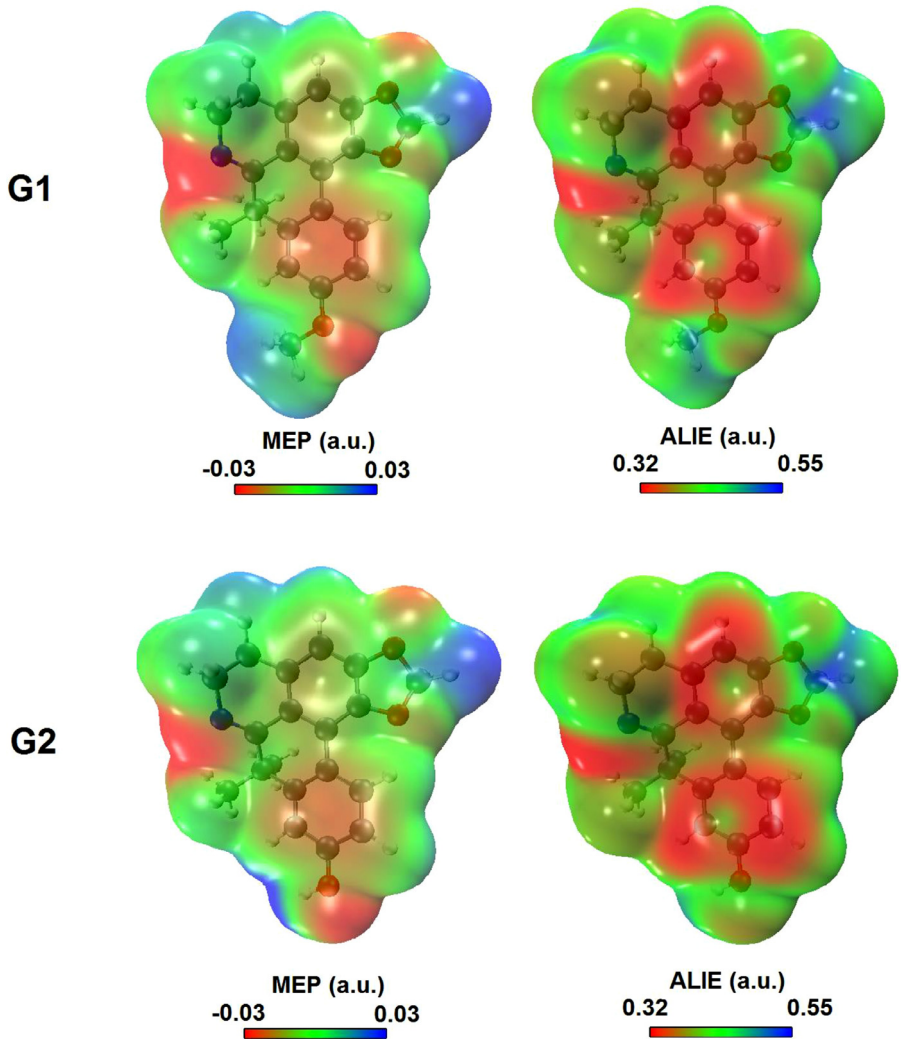

Fig. 3. Calculated MEP and ALIE surfaces for G1 and G2 at B3LYP/6–311G++(2df, 3p).

Table 2
Molecular properties calculated via DFT using 6–311G++(2df, 3p) basis set for G1 and G2.

Quantum chemical parameters	Guadiscine	Guadiscidine
E_{HOMO} (e.V.)	−5.73	−5.81
E_{LUMO} (e.V.)	−1.43	−1.47
$\Delta E_{HOMO\text{-}LUMO}$ (e.V.)	4.30	4.34
Chemical Potential (μ)	3.58	3.64
Hardness (η)	2.15	2.17
Electronegativity (χ)	−3.58	−3.64
Electrophilicity index (ω)	2.98	3.05

However, it is important to emphasize that exchange-correlation functionals are continuous approximations, which does not provide accurate orbital energies. In molecular orbital theory approaches, small HOMO-LUMO gap indicates a soft molecule and reflects a more reactive molecule, whereas a large gap represents a hard and more stable molecule [38]. The electrophilicity index (χ) allows the classification as strong ($\omega >$ 1.5 eV), poor ($\omega <$ 0.8 eV) and moderate (intermediate values) electrophile for a certain molecule [39-41]. The chemical potential measures the tendency of change transfer, since the system always tends to a lower chemical potential [41].

Table 2 presents these parameters values calculated for G1 and G2 molecules via DFT using B3LYP/6–311G++(2df, 3p) level. As seen in Fig. 2, the calculated HOMO, for both structures, comprises rings A and C and atom O3, while the calculated LUMO comprises almost the entirely structures, with the exception of carbons 4, 5 and 12 and the methyl groups in position 7. The analysis of the obtained global reactivity values does not allow to affirm that one is more reactive than the other, but both have similar reactivity and thus similar biological activity. However, comparing these hardness values with the calculated ones for other know aporphine alkaloids that present biological activity, like liriodenine (η= 1.81 eV) [42], 9-methoxyguatterfriesine (n = 2.02 eV) and 4,5-dehydro-9-methoxyguatterfriesine (η= 1.88 eV) [14], G1 and G2 can be classified as soft molecules. The obtained electronegativity (χ) and electrophilicity index values (ω) showed that both molecules can act as excellent nucleophiles.

3.3. MEP and ALIE analysis

The electrostatic potential is a powerful tool that provides insights into regions susceptible to interact with charged species, in studies of biological recognition, interactions between the same molecules (*e.g.*, forming dimers and clusters) or with other molecules and in the evaluation of drug molecules properties and their analogs, being helpful in drug design [43]. As shown in Fig. 3,

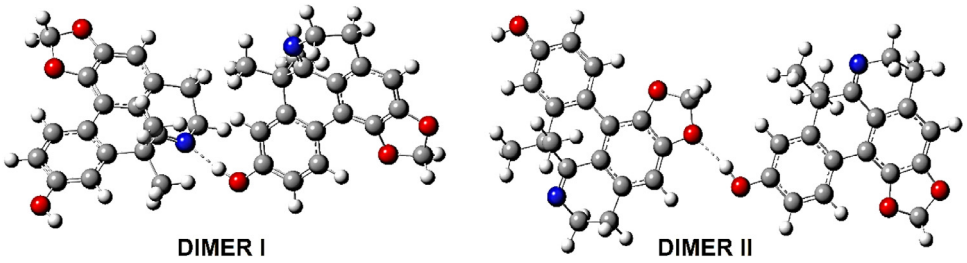

Fig. 4. Proposed dimers for G2.

G1 MEP showed negative regions over ring D (−0.023 a.u.), N6 (−0.042 a.u.), O1 (−0.022 a.u.) and O3 (−0.027 a.u.) atoms. Positive potentials were registered over CH_2 (0.025 a.u.) and over CH_3 bonded to O3 atom (0.019 a.u.). G2 presents its most positive region over hydrogen atom of OH group (0.058 a.u.) and over CH_2 group of the five-membered ring (0.026 a.u.). The most negative potential regions occur over N6 (−0.040 a.u.), O3 (−0.031 a.u.) and O1 (−0.020 a.u.) atoms and over ring D (−0.020 a.u.).

Average local ionization energy (ALIE) surfaces reports electron withdrawing energy values over the molecular surface, helping in the prediction of sites prone to receive electrophilic attack. The analysis of these surfaces is quite simple, red zones indicate regions where electrons are easier to remove, while blue regions indicates zones which the electron's removal requires great amount of energy [44]. For both molecules, ALIE surface analysis reveals that regions over rings A and D are more prone to suffer electrophilic attacks (0.32 a.u.), while oxygen atoms showed higher values (~0.40 a.u.), indicating that they are more prone to interact electrostatically with positively charged species than suffer electrophilic attacks (O3 atom of G2 showed a lower value in relation to the O3 atom of G1). The basicity of N6 atom was confirmed in both structures, which is verified by the low energy value (0.33 a.u.) over N6 in ALIE surfaces, indicating that N6 electron pair are less tightly-held to the nucleus. However, it should be noted that the region over the double bond has a higher average energy (0.40 a.u.), indicating resonance of the group N6=C6a with ring A, suggesting these alkaloids to be mildly basic.

Guided by the opposite potentials, dimers were proposed for G2, as depicted in Fig. 4. The stability of the proposed dimers were evaluated by ΔE (interaction energy value), defined as $\Delta E = E_{DIMER} - 2E_{MONOMER}$, where the obtained values were −11.10 and −6.11 kcal/mol for dimers I and II, respectively, at B3LYP/6–311G(2d, p). Applying the counterpoise correction, the corrected ΔE values were −8.28 and −3.40 kcal/mol, respectively, revealing stability for the proposed dimers in gas phase.

3.4. Fukui function

Fukui function is commonly used in quantum-mechanics calculations to investigate local reactivity on molecular systems, helping in predict sites prone to suffer nucleophilic , electrophilic or radical attack. The Fukui function was defined by Parr and Yang in 1984 as [45]:

$$f(r) = \left[\frac{\delta^2 E}{\delta v(r)\partial N}\right] = \left(\frac{\partial \rho(r)}{\partial N}\right)_v$$

Due to the fact that $\rho(r)$, as a function of ***N,*** like *E(N),* has slope discontinuities, this definition provides three local reaction descriptors (LRD), governing nucleophilic (f^+), electrophilic (f^-) and radical (f^0) attacks, defined as:

$$f^-(r) = \rho_N(r) - \rho_{N-1}(r)$$
$$f^+(r) = \rho_{N+1}(r) - \rho_N(r)$$
$$f^0(r) = \tfrac{1}{2}[\rho_{N+1}(r) - \rho_{N-1}(r)]$$

where $\rho N{+}1(r)$, $\rho N(r)$ and $\rho N{-}1(r)$ correspond to the electronic density of the anion, neutral and cationic chemical species respectively.

Due to the discontinuity of $f(r)$, Yang and Mortier [46-49] demonstrated a simple procedure to calculate Fukui indices condensed to individual atoms in a molecule:

$$f_k^-(r) = q_k(N-1) - q_k\ (N)$$
$$f_k^+(r) = q_k(N) - q_k\ (N+1)$$
$$f_k^0(r) = \tfrac{1}{2}[q_k(N-1) - q_k\ (N+1)]$$

where q is the net charge on the k-th atom whose nuclear charge is Z_K on the k-th atom in the neutral (N), anionic ($N + 1$) or cationic (N-1) chemical species.

Another important LRD is the dual descriptor $f^2(r)$, proposed by Morell et al. [50], which describes both nucleophilic and electrophilic sites of a molecule, defined as:

$$f^2(r) = \left(\frac{\partial^2 \rho(r)}{\partial N^2}\right)_v = \left(\frac{\partial f(r)}{\partial N}\right)_v = \left[\frac{\delta \eta}{\delta v(r)}\right]_N$$

The difference between nucleophilic and electrophilic Fukui indices leads to an approximation for $f^2(r)$, which is:

$$f^2(r) \approx f^+(r) - f^-(r) = \rho_{N+1}(r) - 2\rho_N + \rho_{N-1}$$

The dual descriptor allows obtaining simultaneously the preferable sites for nucleophilic attacks ($f^2(r) > 0$) and electrophilic attacks ($f^2(r) < 0$) on the molecular system, being more reliable for predicting the reactive sites, since $f^2(r)$ discards ambiguities [51].

Fig. 5 shows the calculated Fukui indices surfaces for G1 and G2 at the B3LYP/6–311G(2d, p) level. In the case of a nucleophilic attack, both molecules exhibit prone reactive sites on C2, C3, N6, C7a, C9 atoms and on C3-C6a, C1-C11a double bonds. Regions susceptible to electrophilic attacks are located on rings A and C, specifically on C1a=C1, C11a=C7a and C10=C4 double bonds and O1, C3, O3 and C3a atoms. Concerning to the $f^0(r)$ descriptor, the most reactive sites in face of a free radical attack are on C1, C10, O11, O18, O20 atoms and C2=C6 and C3=C4 bonds. In Fig. 6, the calculated $f^2(r)$ isosurfaces reveals that C1a atom is predominantly electrophilic due to the positive isovalue in both structures. Also, confirmed that N6, C6a, C2 atoms are electrophilic centers, while C1, C11a and O3 atoms are predominantly nucleophilic. Table 3 summarizes the condensed atomic Fukui function approximation, using NBO charges (Natural population analysis). The condensed atomic approximation values reveals, for both molecules, that N6a has the highest $f^+{}_k$ value, followed by C2, C1a, C6a and C9 atoms, while C1 atom shows the highest $f^-{}_k$ value, followed by C11a, C9, O3, O2 and C3a atoms. $f^2{}_k$ descriptor shows that C2 and C6a atom presents the highest values, followed by C1a and N6 atoms, being electrophilic centers, while C1 and C11a atoms present the lowest values, followed by O3 and C3a atoms, thus, being nucleophilic centers. C9 atom, which showed highest values for both $f^+{}_k$ and $f^-{}_k$ descriptors, presented a practically null $f^2{}_k$ value. These results justify the follow experimental observations: that G1 is obtained from G2 through an O-methylation, which preferably occurs

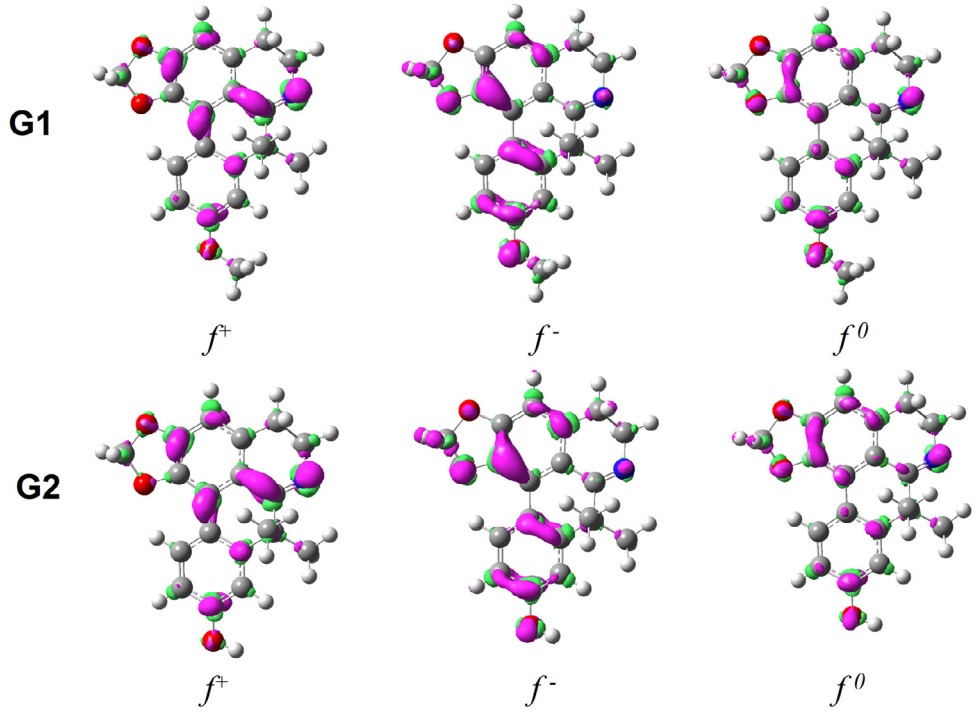

Fig. 5. Nucleophilic (f^+), electrophilic (f^-) and radical (f^0) Fukui functions surfaces generated at isovalue 0.0035 a.u., via DFT B3LYP/6–311 G (2d, p) level of theory, for guadiscine (G1) and guadiscidine (G2).

Table 3
Values of the Fukui indices considering Natural Population analysis (NPA).

Guadiscine (G1) Atom	$q_k\ (N+1)$	$q_k(N)$	$q_k(N-1)$	${f^+}_k$	${f^-}_k$	${f^2}_k$	${f^0}_k$
C1	0.269	0.269	0.354	0.001	0.085	−0.085	0.043
C2	0.213	0.297	0.300	0.084	0.003	0.081	0.044
C3	−0.320	−0.261	−0.214	0.059	0.047	0.012	0.053
C3a	0.013	0.026	0.091	0.013	0.065	−0.052	0.039
C3b	−0.166	−0.115	−0.110	0.051	0.005	0.046	0.028
C1a	−0.132	−0.050	−0.042	0.082	0.008	0.074	0.045
O1	−0.564	−0.534	−0.494	0.030	0.040	−0.010	0.035
O2	−0.567	−0.552	−0.486	0.015	0.066	−0.051	0.041
C6a	0.245	0.306	0.288	0.061	−0.018	0.079	0.022
C11a	−0.091	−0.092	−0.008	−0.001	0.084	−0.085	0.042
N6	−0.588	−0.481	−0.433	0.107	0.048	0.059	0.077
C7a	−0.024	0.036	0.080	0.060	0.044	0.016	0.052
C8	−0.301	−0.300	−0.273	0.001	0.027	−0.026	0.014
C9	0.279	0.351	0.419	0.072	0.068	0.004	0.070
C10	−0.275	−0.243	−0.194	0.032	0.049	−0.017	0.041
C11	−0.172	−0.153	−0.146	0.019	0.007	0.012	0.013
O3	−0.546	−0.528	−0.454	0.018	0.074	−0.056	0.046

Guadiscidine (G2) Atom	$q_k\ (N+1)$	$q_k(N)$	$q_k(N-1)$	${f^+}_k$	${f^-}_k$	${f^2}_k$	${f^0}_k$
C1	0.270	0.269	0.373	−0.001	0.104	−0.105	0.052
C2	0.211	0.298	0.305	0.087	0.007	0.080	0.047
C3	−0.319	−0.260	−0.222	0.059	0.038	0.021	0.048
C3a	0.012	0.025	0.103	0.013	0.078	−0.065	0.046
C3b	−0.166	−0.115	−0.109	0.051	0.006	0.045	0.028
C1a	−0.133	−0.050	−0.039	0.083	0.011	0.072	0.047
O1	−0.564	−0.534	−0.487	0.030	0.047	−0.017	0.038
O2	−0.567	−0.551	−0.478	0.016	0.073	−0.057	0.045
C6a	0.241	0.305	0.289	0.064	−0.016	0.080	0.024
C11a	−0.092	−0.093	−0.019	−0.001	0.074	−0.075	0.036
N6	−0.590	−0.480	−0.429	0.110	0.051	0.059	0.081
C7a	−0.019	0.034	0.075	0.053	0.041	0.012	0.047
C8	−0.293	−0.290	−0.265	0.003	0.025	−0.022	0.014
C9	0.295	0.360	0.425	0.065	0.065	0.001	0.065
C10	−0.285	−0.256	−0.214	0.029	0.042	−0.013	0.035
C11	−0.172	−0.149	−0.136	0.023	0.013	0.010	0.018
O3	−0.706	−0.677	−0.609	0.029	0.068	−0.039	0.0485

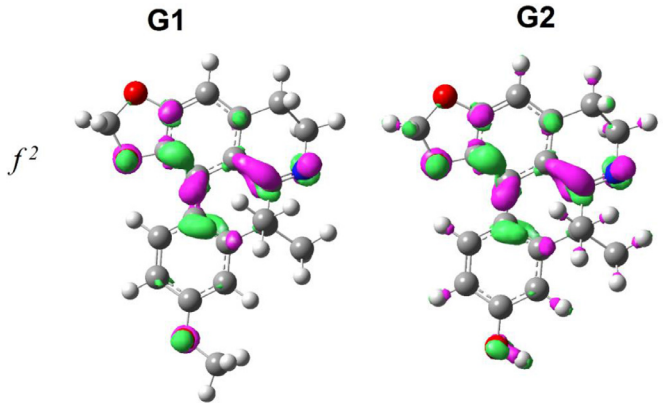

Fig. 6. Dual descriptor (f^2) surfaces generated at isovalue 0.0035 a.u., via DFT B3LYP/6–311 G (2d, p) level of theory, for guadiscine (G1) and guadiscidine (G2). Dual descriptor is a biphasic function, the positive phase (magenta lobes) indicates electrophilic centers and the negative phase (light green lobes) indicates nucleophilic centers. (For interpretation of the references to colour in this figure legend, the reader is referred to the web version of this article.)

on G2's O3 atom [52]; 6,6a-dihydrodemethoxy-aporphine alkaloids could be obtained from G1/G2 through imine reduction using potassium borohydride [53], where a hydride is transferred to the carbon of the C6a=N6 double bond. This is the case of (*R*)−6,6a-dihydro-9-methoxyguatterfriesine, 6,6adihydroguatterioliscine and 6,6a-dihydrodemethoxy-guadiscine alkaloids, which seems to be obtained from G1/G2 through imine reduction by NADPH [54,55].

3.5. IR analysis

Tables S1 and S2 show the experimental and theoretical wavenumbers obtained for structures G1 and G2 at B3LYP/6–311 G (2d, p) along with potential energy distribution values (PED), where a scale factor of 0.96 was used for theoretical frequencies below 1800 cm^{-1}, and 0.98 for theoretical frequencies above 1800 cm^{-1}. The comparison between the experimental and calculated IR spectra are shown in Figs. 7 and 8. The differences between the theoretical and experimental spectra occur due the fact that theoretical DFT calculations are made in the gas phase, while experimentally, the molecules are in solid state. Also, anharmonic vibrations occur in experimental spectra. The assignment of the experimental bands of G1 showed that modes in the 3000–2800 cm^{-1} region are related to H–C stretching (bands at 2925 and 2849 cm^{-1} that corresponds to the theoretical scaled wavenumbers 2920.42 and 2860.53 cm^{-1}) of ring B and methyl group C14. Bands in the 1700–1000 cm^{-1} region were related to stretching of N6=C6a (band at 1635cm^{-1} that corresponds to calculated theoretical scaled wavenumber 1649.77 cm^{-1}), C=C groups on rings A and C (bands at 1608, 1573, 1511 and 1282 cm^{-1} that correspond to the theoretical scaled wavenumbers 1603.64, 1572.82, 1511.19 and 1279.79 cm^{-1}), bending vibration modes of H–C—H (bands at 1511, 1459, 1442, 1380 and 1186 cm^{-1} that correspond to the theoretical scaled wavenumbers 1511.19, 1459.54, 1446.58, 1390.34 and 1186.96 cm^{-1}) and H–C—C groups (bands at 1312, 1250 and 1229 cm^{-1} corresponding to the theoretical scaled wavenumbers at 1308.44, 1248.44 and 1228.51 cm^{-1}) and torsion modes of H–C—O–C groups (band at 1186 cm^{-1} that assigned to the theoretical wavenumber 1186.96 cm^{-1}). Bands between 1000–700 cm^{-1} are mostly related to O–C stretching (dioxomethylene portion), H–C—C–C torsion and C=C stretching.

For structure G2, the IR analysis showed that modes in the 3600–2800 cm^{-1} region are related to O–H stretching (band at 3422 cm^{-1} that corresponds to the theoretical scaled wavenumber 3669 cm^{-1}) and H–C stretching, mainly of ring B and methyl groups C14 and C13 (bands at 2960, 2922 and 2849 cm^{-1} that correspond to the theoretical wavenumbers 2971.40, 2921.09 and 2860.82 cm^{-1}). Bands in the 1700- 1000 cm^{-1} region were assigned to the stretching of N6=C6a (band at 1636cm^{-1} that corresponds to calculated theoretical scaled wavenumber 1650.48 cm^{-1}), C=C groups on ring A (bands at 1599 and 1383 cm^{-1} that corresponds to the theoretical scaled wavenumbers 1600.27 and 1369.55 cm^{-1}), bending vibration modes of H–C—H (bands at 1513, 1460, and 1399cm^{-1} that correspond to the theoretical scaled wavenumbers 1519.22, 1462.43 and 1390.92 cm^{-1}), H–C—C (bands at 1336, 1249 and 1226 cm^{-1}, that correspond to the theoretical scaled wavenumbers at 1328.82, 1253.82 and 1228.21 cm^{-1}) and H–O—C groups (band at 1336 cm^{-1}, assigned to the theoretical wavenumber 1328.82 cm^{-1}), C=C stretching (bands at 1420, 1336

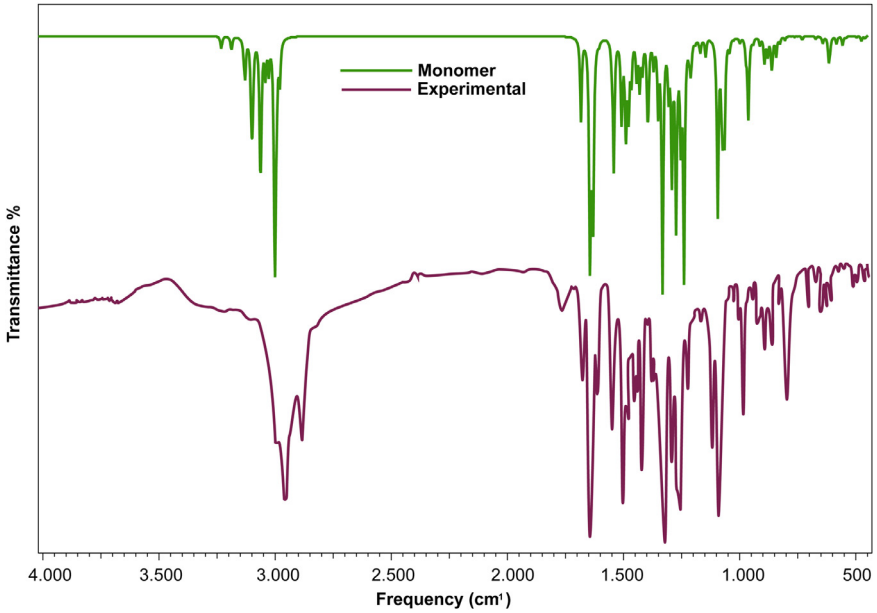

Fig. 7. Comparison between theoretical and experimental infrared spectra of G1. (For interpretation of the references to colour in this figure legend, the reader is referred to the web version of this article.)

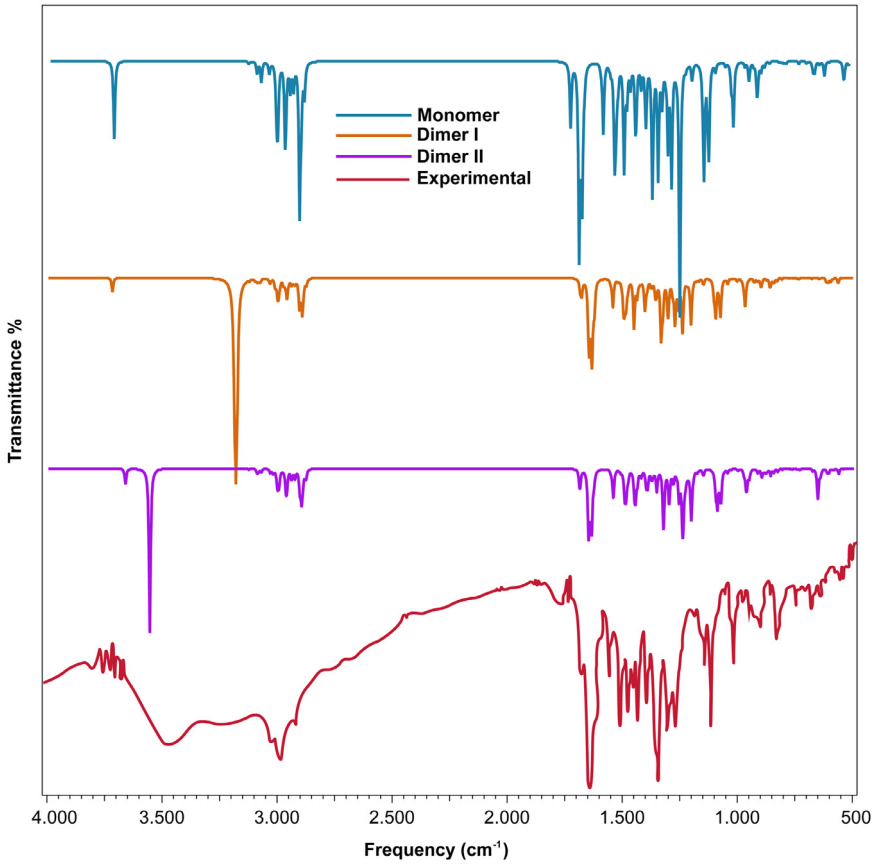

Fig. 8. Comparison between theoretical and experimental infrared spectra of G2. (For interpretation of the references to colour in this figure legend, the reader is referred to the web version of this article.)

and 1286 cm^{-1}, which correspond to the theoretical wavenumbers 1418.86, 1328.82 and 1291.55 cm^{-1}) and O–C stretching vibration modes (band at 1049 cm^{-1} which corresponds to the theoretical wavenumber 1051.23 cm^{-1}). Bands between 1000–700 cm^{-1} are mainly related to O–C stretching and O–C—O bending of dioxomethylene portion and H–C—C–C torsions.

In the 3600–3200 cm^{-1} region, the theoretical wavenumber related to OH stretching is very different than the experimental band at 3422 cm^{-1}, indicating dimer formation. The analysis of the calculated vibrational modes for the proposed dimers (see Fig. 4) did not reveal any significant differences up to 1700 cm^{-1} when compared to monomer, however, in the 3600–3200 cm^{-1} region, the values assigned to O3–H stretching in dimer II shows to be closer to the experimental band at 3422 cm^{-1} (theoretical scaled wavenumbers at 3566.89 cm^{-1} for dimer II and 3668.81 cm^{-1} for the monomer), implying that the intermolecular H-bond O3-H—O1 occur. For dimer I, the O3-H stretching, involved in the intermolecular H-bond O3-H—N6, occur at 3152.75 cm^{-1}, far from the experimental band at 3422 cm^{-1}, but close to the experimental band at 3220 cm^{-1} (small band).

3.6. UV-Vis analysis

The comparison between the UV-Vis spectra of guadiscine (G1) and guadiscidine (G2) in methanol solution and the calculated ones at TD-DFT using B3LYP/6–311G++(2df, 3p) basis set, in methanol (PCM model), are shown in Figs. 9 and 10. Also, the computed UV-Vis electronic absorption wavelengths, oscillator strengths, excitation energies, and major contributions for electronic transitions are listed in Table 4. The experimental spectrum of structure G1 presented bands at 204, 230, 264, 302, 318, 339 and 350 nm, while the theoretical spectrum showed expressive electronic transitions at 218.32 (oscillator strength $f = 0.0518$), 232.62 ($f = 0.0460$), 267.25 ($f = 0.2361$), 276.2 ($f = 0.2833$), 317.8 ($f = 0.1395$) and 339.32 nm ($f = 0.1944$). Major contributions registered for the theoretical bands were H-3 → $L + 1$ (47%) for 218.32 nm, H→ $L + 5$(65.4%) for 232.62 nm, H→ $L + 2$ (50%) for 267.25 nm, H-1→$L + 1$(75.4%) for 276.2 nm, H-1→ L (94%) for 317.8 nm and H→ L (91.6%) for 339 nm (see Figure S19). For G2 molecule, the experimental spectrum showed bands at 206, 230, 266, 304, 318, 342, 352 nm. The theoretical spectrum revealed expressive electronic transitions at 216.87 (oscillator strength $f = 0.0826$), 230.40 nm ($f = 0.0426$ nm), 264.35 nm ($f = 0.2158$), 276.05 ($f = 0.2589$), 315.56 ($f = 0.1532$) and 336.38 nm ($f = 0.1679$), which showed as major contributions the transitions H-1 → $L + 6$ (41%) for 216.87 nm, H-4→L (73.95%) for 230.40 nm, H→ $L + 2$ (52%) for 264.35, H-1→$L + 1$ (71.6%) for 276.05, H-1 → L (93.3%) for 315.56 and H→ L (89.5%) for 336.38 nm (see Figure S20). The analysis of the transitions, reveals, for both alkaloids, that the UV-Vis bands correspond to the sum of the n→π^* and $\pi \rightarrow \pi^*$ transitions involving rings A and D and imine group.

3.7. Molecular docking studies

Guided by the fact that DNA topoisomerases play a key role in DNA topology, such as promoting transient double-strand DNA cleavage, supercoils relaxation and decatenation process, their inhibition is an important factor for the development of chemotherapeutic drugs [56-58]. Also, some articles show that aporphine alkaloids present great antitumor activity [1,2,10,14,16,17], being the trapping of DNA topoisomerase II (DNA-TOPO II) cleavage complex

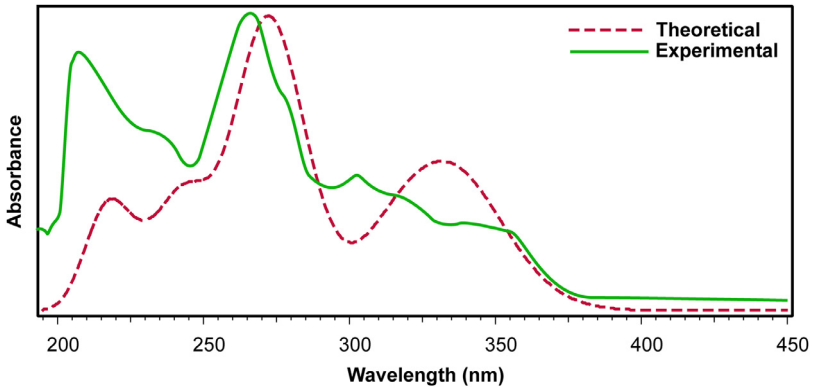

Fig. 9. Comparison between experimental and theoretical UV at B3LYP/6–311G++ (2df, 3p) spectra of G1 in methanol. (For theoretical spectrum, the UV-Vis peak presents a half-width at a half-weight value of 0.19 eV).

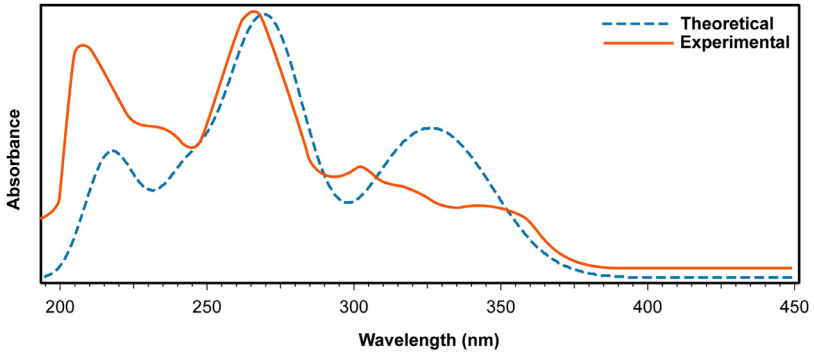

Fig. 10. Comparison between experimental and theoretical UV at B3LYP/6–311G++ (2df, 3p) spectra of G2 in methanol. (For theoretical spectrum, the UV-Vis peak presents a half-width at a half-weight value of 0.19 eV).

Table 4
Experimental and calculated UV–Vis at B3LYP/6–311G++ (2df, 3p). spectroscopic parameters in methanol of G1 and G2 molecules.

Experimental λ (nm)	Theoretical λ (nm)	Oscillator strengths	Excitation energies (eV)	Major contributions
G1				
204	218.32	0.0518	5.6726	H-3→*L* + 1 (46%) + *H*→*L* + 8 (19.8%)
230	232.62	0.0460	5.3298	H→*L* + 5 (65.4%) + *H*→*L* + 4 (14.21%)
264	267.25	0.2361	4.6392	H→*L* + 2 (49.5%) + *H*→*L* + 1 (16.12%) + *H*-3→L (16.13%)
302	276.20	0.2833	4.4889	H-1→*L* + 1 (75.48%)
318	317.80	0.1395	3.9013	H-1→L (94.1%)
339	339.92	0.1944	3.6539	H→L (91.6%)
350	-	-	-	-
G2				
206	216.87	0.0826	5.7171	H-1→*L* + 6 (40.97%) + *H*-3→*L* + 1 (19.2%)
230	230.40	0.0426	5.3812	H-4→L (73.95%)
266	264.35	0.2158	4.6901	H→*L* + 2 (51.96%)
304	276.05	0.2589	4.4914	H-3→*L* + 1 (46%) + *H*→*L* + 8 (19.8%)
318	315.56	0.1532	3.9291	H-1→L (93.3%)
342	336.38	0.1679	3.6858	H→L (89.46%)
352	-	-	-	-

a possible mechanism of action [14,59,60]. In this context, aiming to analyze the inhibitory potential of these alkaloids against the DNA topoisomerase I (DNA-TOPO I) complex, docking calculations were carried out.

Ligand-protein calculations revealed that G1 and G2 showed binding energy values of −8.0 and −8.5 kcal/mol respectively, while topotecan (know inhibitor of DNA-TOPO-I complex) presents a binding energy equal to −12.3 kcal/mol (Figs. 11a and b). Biding mode analysis showed that G1 (guadiscine) complexed with DNA-TOPO-I in the cleavage site by π-π interactions with the base pairs DA 113, DC 112 and TGP 11 (Fig. 11c). Despite the highest binding energy compared to topotecan, the binding modes analysis reveals that rings A and C and dioxomethylene group promote a good interaction with the base pairs, also, the dioxomethylene group allows the formation of a week C–H—O interaction with dexorybose of DA 113. For G2, the presence of a hydroxyl group in position 9 changes the docking pose in the pocket site in relation to G1. Binding modes revealed π-π interactions with DA 113 and DC 112 base pairs, N–H—π interaction between DA 113 and dioxomethylene and ring A , alkyl-π interaction between DC 112 and methyl group, and weak C–H—O hydrogen bond between C5-H and Tyr 426 (Fig. 11d).

3.8. Molecular dynamic simulations

3.8.1. Solvation free energy calculations

The solvation free energy, or hydration free energy (if the solvent is water) is of great use in the material, biological and phar-

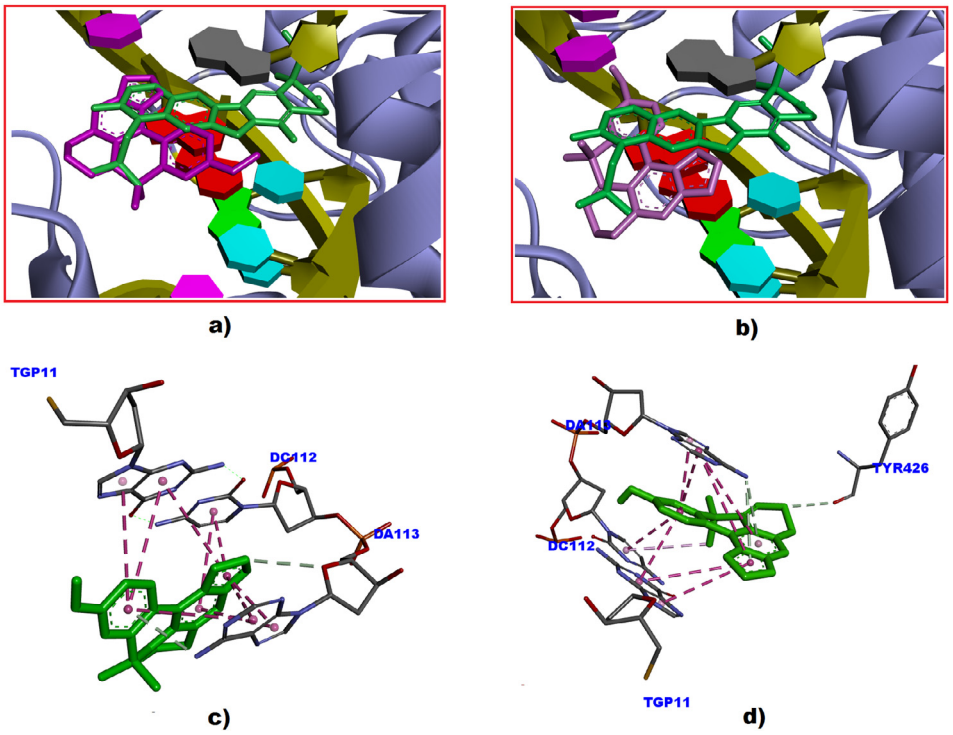

Fig. 11. Docking simulations of G1 (guadiscine) and G2 (guadiscidine) in the DNA-TOPO-I complexes active sites: Superimposition of the docked G1 (magenta) and co-crystallized structure of topotecan (green) (a); Superimposition of the docked G2 (pink) and co-crystallized structure of amsacrine (green) (b); G1-DNA-TOPO I complex interactions (c); G2-DNA-TOPO II complex interactions (d). (For interpretation of the references to colour in this figure legend, the reader is referred to the web version of this article.)

maceutical sciences. In pharmacology, the solvation free energy has its importance because directly affects the bioactivity of a such compound, since the bioorganic processes occur in aqueous medium [61]. Also, in case of naturally occurring bioactive compounds, the determination of solvation free energy is very important in the initial stage of drug discovery, due to the fact that the extraction process depends on the compound's solubility.

The solvation free energy of the molecules was calculated using the methodology for hydration-free energy calculations developed by Klimovich et al. [62]. In this method is calculated the solvation free energy by modifying the solute molecule in each of its environments, through the calculation of the free energy of turning off the solute's non-bonded interactions with its environment (called decoupling), in a series of steps by introducing a parameter λ, which modulates the potential energy of the system. The $\Delta G_{solvation}$ is obtained by a thermodynamic cycle consisted in four parts: (a) a molecule present alone in the gas phase interacting with the surround molecules, (b) the molecule again alone non-interacting with the gas phase molecules, (c) the molecule in a box of water but not interacting with the surrounding water, (d) the same molecule in a box of water interacting with the surrounding molecules, where the pathway is a $\rightarrow$b $\rightarrow$ c $\rightarrow$d. However, the intermolecular interactions of the gas phase were not calculated, as the calculation occur in vacuum. As a result, the free energy change is broken down into two components, the van der Waals (ΔG_{vdW}) and Coulombic (ΔG_{Coul}) contributions of the decoupling process, being $\Delta G_{solvation} = \Delta G_{vdW+}\Delta G_{Coul.}$ For the simulations, Multistate Bennett Acceptance Ratio (MBAR) was used to calculate the free energies for each perturbation. The solvation free energy results for the tested solvents (water, methanol and ethanol), as well as their Coulomb and van der Waals contributions, are shown in Fig. 12 with their corresponding error estimates.

For the studied molecules, it's observed that the solvation free energies present negative values for all the tested solvents, where the magnitude of the solvation-free energy is described in the order water<methanol<ethanol, thus, indicating that the solutes are more soluble in ethanol and methanol than in water. The ΔG_{Coul} values shows, for both molecules, that in water the free energy change is slightly more favorable . The van der Waals effects (ΔG_{vdW}) revealed to be more favorable in ethanol and methanol than in water, but in a higher magnitude, indicating that the van der Waals effect is the determining factor for the greater solvation of these molecules in methanol and ethanol. Comparing the two molecules, guadiscidine (G2) shows greater solvation in all the tested solvents, a fact that is justified by the presence of the OH group, which allows the formation of more H-bonds with the solvents. Moroever, the $-OCH_3$ group of guadiscine (G1) allows the formation of H-bonds with the solvents too. To better understand the interactions between the studied molecules and the solvents it's necessary to appeal to radial distribution function calculations (see next section).

3.8.2. Radial distribution function analysis

Radial distribution function, *g(r)*, describes how the density of the surrounding solvent molecules varies as a function of a distinct point in the molecule, considering the forces that they exert on each other. Fig. 13 shows the most relevant solute-solvent radial distribution function of the interaction between oxygen, nitrogen and hydrogen (G2 hydroxyl group only) atoms of each molecule with the hydrogen and oxygen atoms of each tested solvent (water, methanol and ethanol). For atoms that play a similar role (such as water hydrogen atoms), only one was used as reference for the calculation and not the average *g(r)* of each, since the average relative deviation from the average *g(r)* of similar atoms was less than 2%.

Concerning to the solute-solvent interaction between the studied alkaloids and water (Fig. 13a-b), the N—H and O—H distances are well established for distances at 2 Å, highlighting the inter-

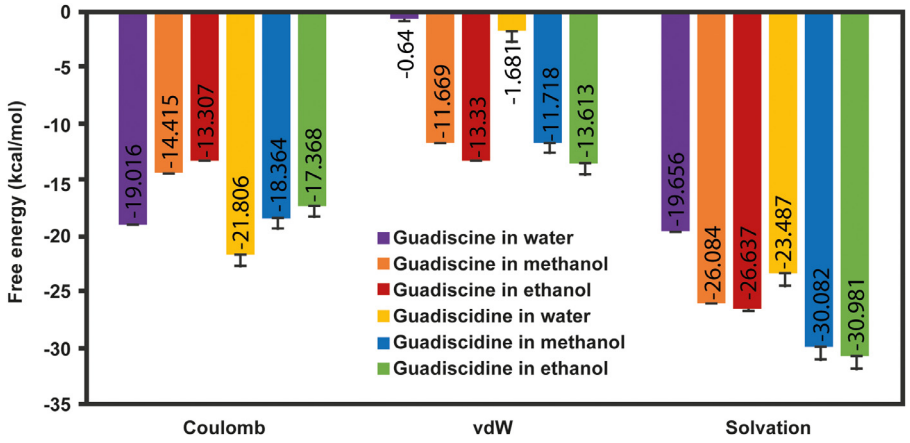

Fig. 12. Total solvation free energy with the contributions of Coulomb and van der Waals interactions and the associated margin of error for the analyzed molecules.

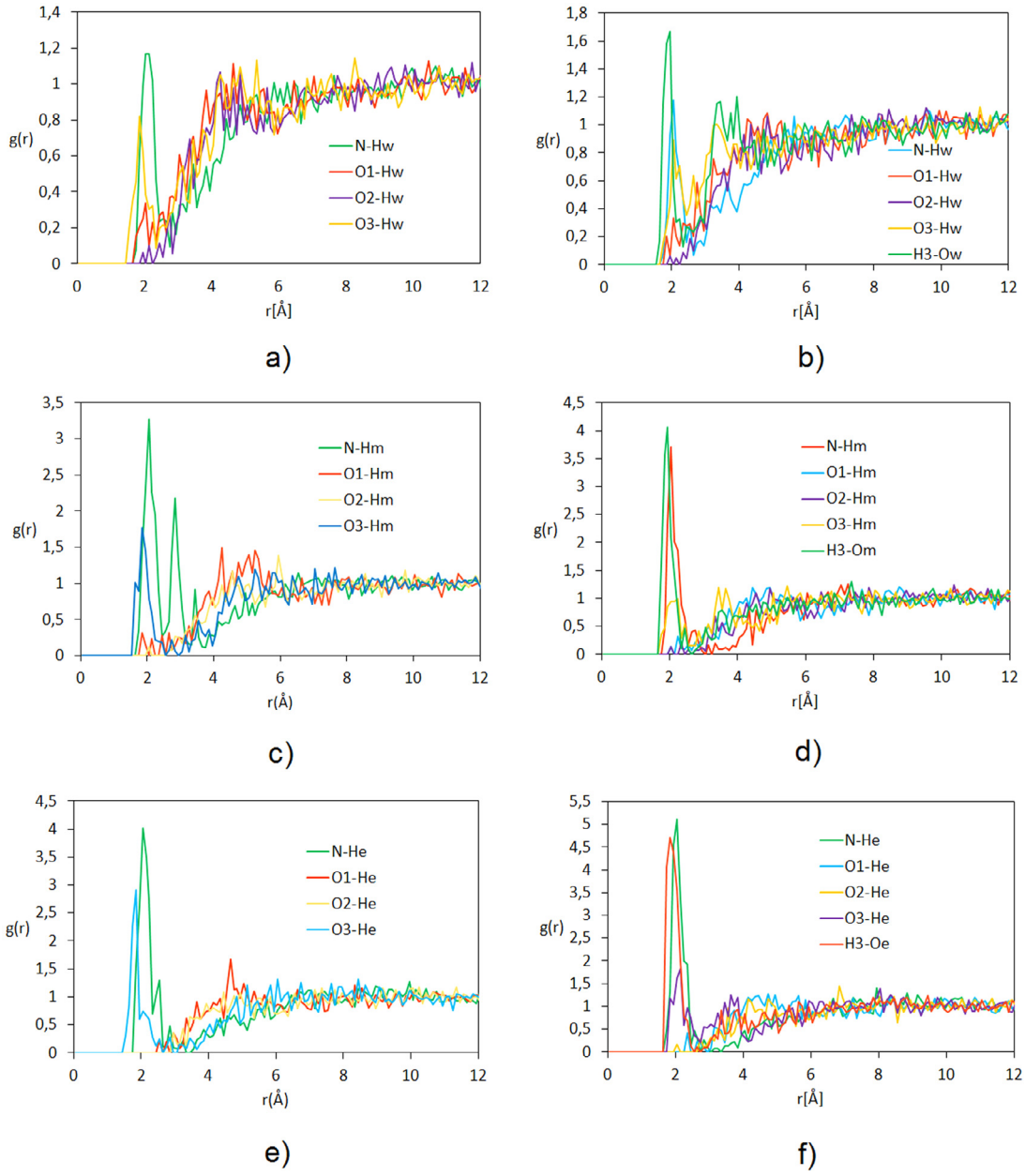

Fig. 13. Solute-solvent radial distribution function of the interaction between selected atoms of the studied molecules and solvents: water and G1(a) and G2 (b) atoms; methanol and G1 (c) and G2 (d) atoms; ethanol and G1(e) and G2 (f) atoms.

action between G2' H3 atom and water oxygen (Fig. 13b), which showed the highest peak, *g(r)* value around 1.75, indicating a stable intermolecular H-bond. Both alkaloids showed expressive peaks for the interaction between nitrogen and water hydrogen, however, the *g(r)* value around 1.15 reveals a moderate concentration of water hydrogen around the nitrogen atom, indicating moderate electrostatic interaction, justifying the moderate basicity of these structures. In MEP and ALIE analysis, was showed that the nitrogen electron pair is less tightly-held to the nucleus, however, the presence of two methyl groups (hydrophobic) in position 7 prevent the formation of higher coordination shells, justifying the *g(r)* results (see section 3.3). Also, for both structures, a weak H-bond was registered between O3 atom and hydrogen water atom at 2 Å, with peak height around 0.8, which is justified by the fact that this atom acts as an electron donor of ring A, presenting low electron density, and, therefore, not acting as a good H-bond receptor.

For the solute-solvent interaction between the aporphine alkaloids and methanol (Fig. 13c-d), the N—H and O—H distances showed high peaks at 2 Å, highlighting the interactions between G2 H3 atom and methanol hydrogen and between G2 nitrogen atom and methanol hydrogen, which showed the highest peaks (Fig. 13d). G1 molecule showed stable intermolecular N—H_m hydrogen bond, presenting two coordination shells, one at 2 Å and other at 3 Å, with peak height values of 3.25 and 2.25, greater than those resulting from the interaction with water hydrogens (Fig. 13c). For both molecules, the O3—H_m interaction showed greater value than those obtained in the aqueous medium too . These results find justification in the presence of two methyl groups in position 7, which interacts with the hydrophobic portion of the methanol molecules, increasing the coordination shell around these atoms in both molecules. O1—H and O2—H interactions practically showed no significant values with the tested solvents. The explanation for this phenomenon lies in the molecular volume of solvent molecules, avoiding a better interaction with O2 atom, whereas for O1 atom, the resonance with ring A makes the electron pairs less available to the medium. For the solute-solvent interaction between the aporphine alkaloids and ethanol (Fig. 13e-f), a pattern similar to that of solutes in methanol was observed, reveling slightly higher peaks at 2 Å for N—H_e, O3—H_e and H3—O_e (only for G2) interactions, due to the increasing of the apolar interactions between methyl groups in position 7 and the -CH_2–CH_3 portion of solvent molecule. These results explain the greater solubility of the studied molecules in methanol and ethanol than in water.

3.9. Cytotoxicity assay

The cytotoxicity of the alkaloids was evaluated against the HepG2 cell line through the alamar blue assay after 72 h of incubation. The IC_{50} values found were 8.27 and 8.28 μM for G1 (guadiscine) and G2 (guadiscidine), respectively, indicating moderate cytotoxic action. Doxorubicin was used as a positive control and had an IC_{50} value of 0.43 μM. These data corroborate with docking calculations and confirm the anticancer potential of these alkaloids. In addition, these data reveal that the presence of a methoxyl or hydroxyl group at position 9 is not important for the cytotoxic activity of these molecules against the HepG2 cell line. However, the presence of the dioxomethylene group (bonded to ring A) enhances the cytotoxic activity, since, in our previous study, the IC_{50} value recorded for the alkaloid 9-methoxyguatterfriesine (6,6a-dehydro-7,7-dimethylaporphine alkaloid that does not has dioxomethylene ring) was higher (IC_{50} = 43.12) [14]. In fact, dioxomethylene ring provides a better DNA intercalation, avoiding (more efficiently) the DNA cleavage process by topoisomerase enzymes.

4. Conclusions

The aporphine alkaloids guadiscine (G1) and guadiscidine (G2), previously isolated from *G. friesiana* were comprehensively studied, with their structure, quantum properties, spectral behavior (IR and UV-Vis) and solvation in different solvents analyzed via DFT and MD calculations. MEP and ALIE surfaces allowed the visualization of the best sites for protonation, also the proposition of dimers for G2 molecule. The IR study revealed several characteristic vibrations that helps the characterization of the 6,6a-dehydro-7,7-dimethylaporphines, also, the comparison between calculated and experimental wavenumbers revealed that dimers showed O–H stretching vibrations more close to the experimental bands than the monormers in the 4000–3200 cm^{-1} region, implying that the proposed dimers are plausible. Fukui functions analysis showed that C2, C6, C1a and N6 atoms are prone to nucleophilic attack, while C1, C11a, O3 and C3a atoms are prone to electrophilic attack. The *in vitro* cytotoxicity results against HepG2 cell line showed IC_{50} values of 8.27 and 8.28 μM for G1 (guadiscine) and G2 (guadiscidine), respectively, confirming the antitumor potential for these alkaloids. Furthermore, docking calculations performed with DNA-topoisomerase I complex indicate that the studied molecules are good topoisomerase I inhibitors. MD simulations showed that G1 and G2 alkaloids are better solvated in methanol and ethanol, indicating that these solvents are better for the extraction of this type of molecule, however, the solvation free energy values in water, which were −19.6 and −23.5 kcal/mol respectively, corroborate their pharmacological potential.

Declaration of Competing Interest

The authors declare that they have no known competing financial interests or personal relationships that could have appeared to influence the work reported in this paper.

Acknowledgments

The authors are grateful to Conselho Nacional de Desenvolvimento Científico e Tecnológico (CNPq), Coordenação de Aperfeiçoamento de Pessoal de Nível Superior (CAPES) - Code 001, Financiadora de Estudos e Projetos (FINEP), Fundação de Amparo à Pesquisa do Estado da Bahia (FAPESB), and Federal University of Amazonas (UFAM) for financial support and fellowship.

Supplementary materials

Supplementary material associated with this article can be found, in the online version, at doi:10.1016/j.molstruc.2020.129844.

References

[1] D.B. da Silva, E.C.O. Tulli, G.C.G. Militão, L.V. Costa-Lotufo, C. Pessoa, M.O. de Moraes, S. Albuquerque, J.M. de Siqueira, The antitumoral, trypanocidal and antileishmanial activities of extract and alkaloids isolated from *Duguetia furfuracea*, Phytomedicine 16 (2009) 1059–1063 https://doi.org/, doi:10.1016/j.phymed.2009.03.019.

[2] C.A. Siebra, J.M. Nardin, A. Florão, F.H. Rocha, D.Z. Bastos, B.H. Oliveira, A.M. Weffort-Santos, Potencial antiinflamatório de *Annona glabra*, Annonaceae, Braz. J. Pharmacogn. 19 (2009) 82–88 https://doi.org/, doi:10.1590/S0102-695X2009000100017.

[3] S.K. Tripathi, T. Xu, Q. Feng, B. Avula, X. Shi, X. Pan, M.M. Mask, S.R. Baerson, M.R. Jacob, R.R. Ravu, S.I. Khan, X.C. Li, I.A. Khan, A.M. Clark, A.K. Agarwal, Two plant-derived aporphinoid alkaloids exert their antifungal activity by disrupting mitochondrial iron-sulfur cluster biosynthesis, J. Biol. Chem. 292 (2017) 16578–16593 https://doi.org/, doi:10.1074/jbc.M117.781773.

[4] E.V. Costa, P.E.O. da Cruz, C.C. Lourenço, V.R. de S. Moraes, P.C. de L. Nogueira, M.J. Salvador, Natural Product Research : formerly Natural Product Letters Antioxidant and antimicrobial activities of aporphinoids and other alkaloids from the bark of *Annona salzmannii* A . DC . (Annonaceae), Nat. Prod. Res. 27 (2013) 1002–1006 https://doi.org/, doi:10.1080/14786419.2012.688044.

[5] C. Stévigny, C. Bailly, J. Quetin-Leclercq, Cytotoxic and antitumor potentialities of aporphinoid alkaloids, Curr. Med. Chem. - Anti-Cancer Agents. 5 (2005) 173–182 https://doi.org/, doi:10.2174/1568011053174864.T.

[6] F.R. Garcez, A.G. Francisca da Silva, W.S. Garcez, G. Linck, M.C. de Fatima Matos, E.C.S. Santos, L.M.M. Queiroz, Cytotoxic aporphine alkaloids from *Ocotea acutifolia*, Planta Med 77 (2011) 383–387.

[7] M.V.N. Rinaldi, I.E.C. Díaz, I.B. Suffredini, P.R.H. Moreno, Alkaloids and biological activity of beribá (*Annona hypoglauca*), Rev. Bras. Farmacogn. 27 (2017) 77–83 https://doi.org/, doi:10.1016/j.bjp.2016.08.006.

[8] A.Q. Lobão, R. de Mello-Silva, R.C. Forzza, Guatteria (Annonaceae) da Floresta Atlântica brasileira, Rodriguésia 63 (2012) 1039–1064.

[9] J.D. Phillipson, M.F. Roberts, M.H. Zenk, The Chemistry and Biology of Isoquinoline Alkaloids, Springer, Berlin, 1985.

[10] E.V. Costa, F.A. Marques, M.L.B. Pinheiro, N.P. Vaz, M.C.T. Duarte, C. Delarmina, R.M. Braga, 7,7-Dimethylaporphine alkaloids from the stem of *Guatteriopsis friesiana*, J. Nat. Prod. 72 (2009) 1516–1519.

[11] Z. Zhang, H.N. ElSohly, M.R. Jacob, D.S. Pasco, L.A. Walker, A.M. Clark, New sesquiterpenoids from the root of *Guatteria multivenia*, J. Nat. Prod. 65 (2002) 856–859, doi:10.1021/np0200717.

[12] A.A. Ahamd, A.A. Mahmoud, H. J.Williams, A.I. Scott, J.H. Reibebspies, T.J. Mabry, New sesquiterpene-methylene lactones from the Egyptian plants *Jasonia candicans*, J. Nat. Prod. 56 (1993) 1276–1280.

[13] M. Shamma, W.A. Slusarchyk, The aporphine alkaloids, Chem Rev 64 (1964) 59–79.

[14] A.D.S. Branches, R.A. Costa, E.S.A. Junior, D.P. Bezzera, M.B.P. Soares, E.V. Costa, K.M.T. Oliveira, Theoretical and experimental study by DFT, molecular docking calculations and cytotoxicity assay of 7,7-dimethylaporphine alkaloids type isolated from *Guatteria friesiana* (Annonaceae), J. Mol. Struct. 1177 (2019) 347–362 https://doi.org/, doi:10.1016/j.molstruc.2018.09.060.

[15] J.-J. Chen, H.-C. Hung, P.-J. Sung, I.-S. Chen, W.-L. Kuo, Aporphine alkaloids and cytotoxic lignans from the roots of *Illigera luzonensis*, Phytochemistry 72 (2011) 523–532.

[16] C.A.S. de Souza, V.B. Nardelli, W.H.P. Paz, M. L. B. Pinheiro, A.C.B.C. Rodriguesda, L.M. Bonfim, M.B.P. Soares, D.P. Bezerra, S. Chaara J.da, H.H.F. KoolenKoolen, F.M.A. Silva, E. V. Costa, Asarone-derived phenylpropanoids and isoquinoline-derived akaloids from the bark of Duguetia pycnastera (Annonaceae) and their cytotoxicities, Quim. Nova (2020), doi:10.21577/0100-4042.20170617.

[17] E.V. Costa, P.E.O. da Cruz, M. Lúcia B. Pinheiro, F.A. Marques, A. Lúcia T. G. Ruiz, G.M. Marchetti, J.E. de Carvalho, A. Barison, B.H.L.N.S. Maia, Aporphine and tetrahydroprotoberberine alkaloids from the leaves of *Guatteria friesiana* (Annonaceae) and their cytotoxic activities, J. Braz. Chem. Soc. 24 (2013) 788–796.

[18] Gaussian 09, Revision E01, Frisch M.J., Trucks G.W., Schlegel H.B., Scuseria G.E., Robb M.A., Cheeseman J.R., Scalmani G., Barone V., Petersson G.A., Nakatsuji H., Li X., Caricato M., Manerich A., Bloino J., Janesko B.G., Gomperts R. , Mennucci B., Hratchian H.P., Ortiz J.V., Izmaylov A.F. , Sonnenberg J.L., Williams-Young D., Ding F. , Lipparini F. , Egidi F., Goings J., Peng B., Petrone A., Henderson T., Ranasinghe D., Zakrzewski V.G., Gao J., Rega N., Zheng G., Liang W., Hada M., Ehara M. ,Toyota K. , Fukuda R., Hasegawa J., Ishida M., Nakajima T., Honda Y., Kitao O., Nakai H., Vrenen T., Throssell K., Montgomery J.A., Peralta J.E., Ogliaro F. , Bearpark M., Heyd J.J., Brothers E., Kudin K.N., Staroverov V.N., Keith T. , Kobayashi R., Normand J., Raghavachari K., Rendell A., Burant J.C., Iyengar S.S., Tomasi J., Cossi M., Millam J.M., Klene M., Adamo C., Cammi R., Ochterski J.W., Martin R.L., Morokuma K. , Farkas O., Foresman J.B. and Fox D.J., Gaussian, Inc., Wallingford CT, 2016.

[19] T. Lu, F. Chen, Multiwfn: a multifunctional wavefunction analyzer, J. Comp. Chem. 33 (2012) 580–592.

[20] M.H. Jamroz, Vibrational Energy Distribution Analysis VEDA 4, Warsaw, 2004-2010

[21] O. Trott, A.J. Olson, AutoDock Vina: improving the speed and accuracy of docking with a new scoring function, efficient optimization and multithreading, J. Comp. Chem. 31 (2010) 455–461.

[22] C.C. Wu, Y.C. Li, Y.R. Wang, T.K. Li, N.L. Chan, On the structural basis and design guidelines for type II topoisomerase-targeting anticancer drugs, Nucleic Acids Res. 41 (2013) 10630–10640.

[23] R.A. Costa, K.M.T. Oliveira, R.D.C.S. Nunomura, E.S.A. Junior, M.L.B. Pinheiro, E.V. Costa, A. Barison, Quantum chemical properties investigation and molecular docking analysis with DNA topoisomerase II of β -carboline indole alkaloids from Simaba guianensis, Struct. Chem. 29 (2018) 299–314 https://doi.org/, doi:10.1007/s11224-017-1029-5.

[24] R.A. Costa, E.S.A. Junior, J. de A. Bezerra, J. Moreira Mar, E.S. Lima, M.L.B. Pinheiro, D.V.C. Mendonça, G.B.P. Lopes, A.D.S. Branches, K.M.T. Oliveira, Theoretical investigation of the structural, spectroscopic, electronic, and pharmacological properties of 4-nerolidylcathecol, an important bioactive molecule, J. Chem. (2019) Article ID 9627404https://doi.org/, doi:10.1155/2019/9627404.

[25] K. Vanommeslaeghe, E. Hatcher, C. Acharya, S. Kundu, S. Zhong, J. Shim, E. Darian, O. Guvench, P. Lopes, I. Vorobyov, A.D. MacKerell Jr., CHARMM general force field: a force field for druglike molecules compatible with the CHARMM All-Atom Additive Biological Force Field, J. Comput. Chem. 31 (2010) 671–690.

[26] J. Huang, A.D. Mackerell Jr., , CHARMM36 all-atom additive protein force field: validation based on comparison to NMR data, J. Comput. Chem. 34 (2013) 2135–2145.

[27] Abraham M.J., van der Spoel D., Lindhal E., Hess B., and the GROMACS development team, GROMACS User Manual version 2019.

[28] U. Essmann, et al., A smooth particle mesh Ewald method, J. Chem. Phys. 103 (1995) 8577–8593.

[29] B. Hess, H. Bekker, H.J. Berendsen, J.G. Fraaije, LINCS: a linear constraint solver for molecular simulations, J. Comput. Chem. 18 (1997) 1463–1472.

[30] H.J.C. Berendsen, J.P.M. Postma, W.F. van Gunsteren, A. DiNola, J.R. Haak, Molecular dynamics with coupling to an external bath, J. Chem. Phys. 81 (1984) 3684–3690.

[31] L. De Souza Santos, V.R. Silva, L.R.A. Menezes, M.B.P. Soares, E.V. Costa, D.P. Bezerra, Xylopine induces oxidative stress and causes G2/M phase arrest, triggering caspase-mediated apoptosis by p53-independent pathway in HCT116 cells, Oxid. Med. Cell. Longev. (2017) 1–13 https://doi.org/, doi:10.1155/2017/7126872.

[32] J.A. Takahashi, M.B. Floreano, M.S. Oliveira, T.S. Oliveira, J.N. Tabudravu, J.L. Wardell, S.M.S.V. Wardell, Identification and quantification of the fatty acids and isolation of (+)-pinitol, liriodenine, and (−)-*N*-acetyl-anonaine from empty capsules of Michelia champaca fruits. Crystal structure of (−)-*N*-acetylanonaine, Monatsh. Chem. 146 (2015) 1763–1770 https://doi.org/, doi:10.1007/s00706-015-1554-0.

[33] G. Zhang, C.B. Musgrave, Comparison of DFT methods for molecular orbital eigenvalue calculations, J. Phys. Chem. *A* 111 (2007) 1554–1561.

[34] K. Fukui, Role of Frontier Orbitals in Chemical Reactions, Science 218 (1982) 747–754.

[35] N. Flores, J. Frau, D. Mitinik, Conceptual DFT as a novel chemoinformatics tool for studying the chemical reactivity properties of the amatoxin family of fungal peptides, Open Chem. 17 (2019) 1133–1139.

[36] J.F. Janak, Proof that $\partial E\partial ni=\varepsilon i$ in density-functional theory, Phys Rev. B 12 (1978) 7165–7168.

[37] J.P. Perdew, R.G. Parr, M. Levy, J.L. Balduz, Density-functional theory for fractional particle number: derivative discontinuities of the energy, Phys. Rev. Lett. 23 (1982) 1691–1694.

[38] R.G. Parr, R.G. Pearson, Absolute hardness: companion parameter to absolute electronegativity, J. Am. Chem. Soc. 26 (1983) 7512–751699.

[39] R.G. Parr, L.V. Szentpály, S. Liu, Electrophilicity index, J. Am. Chem. Soc. 121 (1999) 1922–1924 https://doi.org/, doi:10.1021/ja983494x.

[40] L.R. Domingo, P. Perez, The nucleophilicity N index in organic chemistry, Org. Biomol. Chem. 9 (2011) 7168–7175.

[41] C.G. Zhan, J.A. Nichols, D.A. Dixon, Ionization potential, electron affinity, electronegativity, hardness, and electron excitation energy: molecular properties from density functional theory orbital energies, J. Phys. Chem. A. 20 (2003) 4184–4195.

[42] R.A. Costa, P.O. Pitt, M.L.B. Pinheiro, K.M.T. de Oliveira, K.S. Salomé, A. Barison, E.V. Costa, Spectroscopic investigation, vibrational assignments, HOMO-LUMO, NBO, MEP analysis and molecular docking studies of oxoaporphine alkaloid liriodenine, Spectrochim. Acta, Part A Mol. Biomol. Spectrosc. 174 (2017) 94–104 https://doi.org/, doi:10.1016/j.saa.2016.11.018.

[43] P.K. Weiner, R. Langridge, J.M. Blaney, R. Schaefer, P.A. Kollman, Electrostatic potential molecular surfaces, Proc. Natl. Acad. Sci. U. S. A. 79 (1982) 3754–3758.

[44] P. Politzer, J.S. Muray, F.A. Bullat, Average local ionization energy: a review, J. Mol. Model. 16 (2010) 1731–1742.

[45] R.G. Parr, W. Yang, Density functional approach to the frontier-electron theory of chemical reactivity, J. Am. Chem. Soc. 106 (1984) 4049–4050.

[46] W. Yang, W.J. Mortier, The use of global and local molecular parameters for the analysis of the gas-phase basicity of amines, J. Am. Chem. Soc. 108 (1986) 5708–5711.

[47] J. Sánchez-Márquez, New advances in conceptual-DFT: an alternative way to calculate the Fukui function and dual descriptor, J. Mol. Model. 25 (2019) 123.

[48] Y. Ma, J. Liang, D. Zhao, Y.-L. Chen, Shen J, B. Xiong, Condensed Fukui function predicts innate C–H radical functionalization sites on multi-nitrogen containing fused arenes, RSC Adv. 4 (2014) 17262.

[49] C.A. Polanco-Ramírez, M. Franco-Pérez, Javier Carmona-Espíndola, J.L. Gázquez, P.W. Ayers, Revisiting the definition of local hardness and hardness kernel, Phys.Chem.Chem.Phys 19 (2017) 12355.

[50] C. Morell, A. Grand, A. Toro-Labbe, New dual descriptor for chemical reactivity, J. Phys. Chem. A 109 (2005) 205–212.

[51] J.I. Martínez-Araya, Why is the dual descriptor a more accurate local reactivity descriptor than Fukui functions? J. Math. Chem. 53 (2015) 451–465.

[52] A. Brossi, in: The Alkaloids: Chemistry and Pharmacology, XXV, Academic Press, Orlando, Florida, 1985, p. 40. pag..

[53] J.D. Phillipson, M.F. Roberts, M.H. Zenk, in: The Chemistry and Biology of Isoquinoline Alkaloids, Springer Verlag, Berlin, 1985, p. 85. pag.

[54] M. Ganda, H. Müller, R. Wardenga, M. Höhne, Characterization of three novel enzymes with imine reductase activity, J. Mol. Cat. B 110 (2014) 126–132.

[55] H. Li, Z.-J. Luan, G.-W. Zheng, J.-H. Xu, Efficient synthesis of chiral indolines using an imine reductase from *Paenibacillus lactis*, Adv. Synth. Catal. 357 (2015) 1692–1696.

[56] M.M. Heck, W.N. Hittelman, W.C. Earnshaw, Differential expression of DNA topoisomerases I and II during the eukaryotic cell cycle, Proc. Natl. Acad. Sci. U S A., 85 (1988) 1086–1090.

[57] M.K. Kathiravan, M.M. Khilare, K. Nikoomanesh, A.S. Chothe, K.S. Jain, Topoisomerase as target for antibacterial and anticancer drug discovery, J. Enzyme Inhib. Med. Chem. 28 (2013) 419–435.

[58] A. Thomas, S. Bates, W.D. Figg Sr, Y. Pommier, DNA topoisomerase targeting drugs,. DNA topoisomerase targeting drugs, Holland-Frei Cancer Med. (2017) 1–17, doi:10.1002/9781119000822.hfcm060.

[59] S.H. Woo, N.J. Sun, J.M. Cassady, R.M. Snapka, Topoisomerase II inhibition by aporphine alkaloids, Biochem. Pharmacol. 15 (1999) 1141–1145, doi:10.1016/s0006-2952(99)00018-0.

[60] S. Hoet, C. Stévigny, S. Block, F. Opperdoes, P. Colson, B. Baldeyrou, A. Lansiaux, C. Bailly, J. Quetin-Leclercq, Alkaloids from *Cassytha filiformis* and related aporphines: antitrypanosomal activity, cytotoxicity and interaction with DNA and topoisomerases, Planta Med. 70 (2004) 407–413.
[61] C.A. Lipinski, F. Lombardo, B.W. Dominy, P.J. Feeney, Experimental and computational approaches to estimate solubility and permeability in drug discovery and development settings, Adv. Drug Deliv. Rev. 23 (1997) 3–25, doi:10.1016/S0169-409X(96)00423-1.
[62] P.V. Klimovich, M.R. Shirts, D.L. Mobley, Guidelines for the analysis of free energy calculations, J. Comput. Aided Mol. *Des.* 29 (2015) 397–411.